A shallow convective model for Jupiter's alternating wind bands

K. L. Chan[1] and H. G. Mayr[2]

Received 21 February 2008; revised 21 July 2008; accepted 30 July 2008; published 3 October 2008.

[1] The dynamics of a thin atmospheric layer (1–340 bar) below the cloud tops of Jupiter is simulated with a three-dimensional, nonlinear transformed spectral model. The gas is compressible and stratified. Commensurate with the observed emitted radiation from Jupiter's atmosphere, the transport of the planet's internal energy in the lower region is taken to be convective, but solar heating is not accounted for. In qualitative agreement with observations, the model produces alternating wind bands and a dominant prograde equatorial jet. The zonal wind speed at the equator is within a factor of 2 of the observed values.

Citation: Chan, K. L., and H. G. Mayr (2008), A shallow convective model for Jupiter's alternating wind bands, *J. Geophys. Res.*, *113*, E10002, doi:10.1029/2008JE003124.

1. Introduction

[2] Despite many years of investigation, the cause for the equatorial jet and alternating wind bands observed on Jupiter (and Saturn) remains a challenging but unsolved problem. It has generally been accepted that fast planetary rotation is an essential ingredient, but the issue about the other required physical factors has not been settled. Existing models can be categorized as two broad types. One is based on the cascade of horizontal, two-dimensional turbulence in a fast-rotating, thin, convectively stable atmosphere [e.g., *Rhines*, 1975; *Williams*, 1978; *Ingersoll and Pollard*, 1982; *Cho and Polvani*, 1996; *Marcus et al.*, 2000; *Yano et al.*, 2003; *Galperin et al.*, 2004; *Showman et al.*, 2006]. The other type of models is based on the influence of fast rotation on three-dimensional convective turbulence [e.g., *Busse*, 1976; *Mayr et al.*, 1984; *Sun et al.*, 1993; *Zhang and Schubert*, 2000].

[3] Most of the earlier models had the problem of not being able to generate the strong prograde jet at the equator. Calculations made by *Christensen* [2001] and *Aurnou and Olson* [2001], however, have changed the situation. Using a spectral approach to simulate incompressible convection in deep rotating shells, they have shown that a strong prograde equatorial jet can be produced if the Rayleigh number is high and the Ekman number is low. Furthermore, *Heimpel and Aurnou* [2007] have shown that alternating wind bands at high latitudes can be produced, if the Reynolds number is high. These simulations have considerably strengthened the position of the convective model.

[4] In this paper, we discuss a model that also treats the layer below the cloud tops as convective, but it is very shallow. The physical situation may be considered as similar to that conceived by *Ingersoll et al.* [2000]. The shallowness makes the model's behavior different from those of earlier convective models. Some characteristics are reminiscent of two-dimensional turbulence models.

[5] In section 2, we describe the numerical model. It has two special features: (1) the atmosphere is compressible and stratified and (2) a realistic energy flux from the interior is applied. Jupiter emits about twice as much energy as it receives from the Sun. Here, solar heating is left out. In section 3, the model results are presented. Interpretation of the results and comparison with previous models are discussed in section 4. A brief summary is given in section 5.

2. Numerical Model

[6] In our model, a spherical shell of gas is considered. The domain depth, d, is 430 km ($\sim$0.6% of the planet's radius, $r_\star$). The pressure range is 1–340 bars. The shell rotates at Jupiter's rate of 1.778×10^{-4} rad/s (Ω). The gas is treated as ideal, i.e., $p = \rho TR/\mu$, where p, ρ, T, R, and μ are the pressure, density, temperature, gas constant, and mean molecular weight, respectively. The value of μ is 2.3; the ratio of specific heats, γ, is taken to be 1.47. The layer below 3.5 bar (fractional radius, $r/r_\star = 0.9995$) is taken as convective, and the layer 1–3.5 bar is convectively stable. The initial distributions of the two layers are taken to be polytropic, i.e., $\rho = T^n$, where n is the polytropic index. The lower layer is initially adiabatic, with $n = 1/(\gamma - 1) = 1.13$. The upper layer has a polytropic index 20% higher, and therefore it is subadiabatic and stable. A constant and uniform energy flux of 5.4 W/m^2 is applied at the bottom boundary, and the temperature at the top of the domain is fixed at 170 K. Radiative transport is handled by the diffusion approximation. In the stable layer, the radiative diffusion coefficient is set to allow the initial temperature gradient to conduct the injected energy flux outward. Convection occurs when radiative transport alone cannot deliver the energy flux from the interior. In the unstable layer, the radiative diffusion coefficient is taken to be zero;

[1]Department of Mathematics, Hong Kong University of Science and Technology, Hong Kong, China.
[2]NASA Goddard Space Flight Center, Greenbelt, Maryland, USA.

Copyright 2008 by the American Geophysical Union.
0148-0227/08/2008JE003124

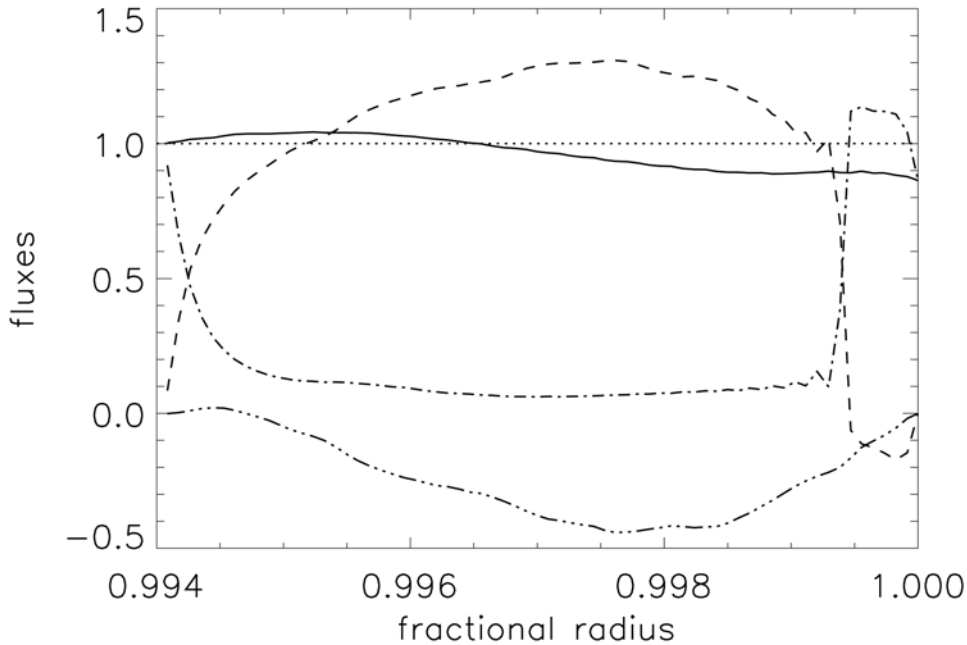

Figure 1. The latitudinally averaged mean energy fluxes versus fractional radius. The enthalpy, radiative, and kinetic energy fluxes are shown by the dashed, dashed-dotted, and dashed-tripple-dotted curves, respectively. The sum of these fluxes is given by the solid curve, and the flux injected at the bottom is shown as the flat dotted line. Above the boundary between the stable and unstable layers, the radiative flux begins to dominate at the expense of the enthalpy flux.

convection is thus generated. An entropy diffusion term (only in the convection zone) is introduced in the energy equation to aid numerical stability. Since the entropy gradient is close to zero in the convection zone, the entropy diffusion flux ($-\kappa\rho C_p T \nabla S$ where κ, C_p, and S are the diffusion coefficient, specific heat under constant pressure, and specific entropy, respectively) is small. The readers are referred to *Chan and Sofia* [1986] (hereinafter referred to as CS86) for a discussion of this technical point. A uniform kinematic viscosity ν of 5.6 m^2/s is adopted to dissipate the kinetic energy generated by convection. The stress-free and impenetrable boundary conditions are applied at both the top and bottom boundaries. In the convection zone, κ is related to ν through the effective Prandtl number $Pr = \nu/\kappa = 1/3$.

[7] The numerical code is based on the transformed spectral method with spherical harmonics. It solves a set of nonlinear equations close to the fully compressible Navier-Stokes equations [*Chan et al.*, 1994]. In the modified equations, the linear terms are left intact. By assuming that the square of the Mach number is small ($M^2 \ll 1$), approximations are introduced only in handling of the nonlinear terms. Let q be any one of ρ, p, or T. It can be written as $q = q_0 + q_1$ where q_0 and q_1 are the horizontal average (over a sphere) and the variation, respectively (both are time-dependent). As the assumption implies that all the q_1/q_0 are small, expansion terms containing second-order or higher powers of such ratios are neglected. In the resultant equation, the nonlinear terms that need to be transformed are of the form velocity $\times$ q_1/q_0 or velocity $\times$ velocity. The nonlinearity is only quadratic so that nonaliasing transformations can be easily accommodated. The conservation of total mass and total angular momentum (with respect to a nonrotating frame) are satisfied to round off.

[8] The solution procedure computes the linear terms implicitly in spectral space, and that improves the stability of the code substantially. The time steps are not restricted by the sound waves and gravity waves associated with these terms. On the other hand, the nonlinear advection terms are calculated explicitly in physical space. The fluid velocity imposes a limit on the time step size. In the present calculation, the Mach number is on the order of 0.1, and the sound speed CFL number (defined by $c\Delta t/\Delta r$, where c is the sound speed, Δt is the time step, and Δr is the radial grid spacing) is typically about 10. With such a restrictive time step size, our thin fluid layer requires about 20 billion steps to reach thermal relaxation, the time scale being $\sim\int e dr/F$ (where e is the internal energy density and F is the energy flux). The readers are referred to CS86 for a discussion of the relaxation issue. The computation is therefore very costly. Presently, we can only afford to compute a T20 $\times$ 68 model (triangular truncation of the spherical harmonics with a maximum degree of 20, and 68 finite difference grid levels in the radial direction). After 200 million steps ($\sim$800 Earth years), rough thermal equilibrium is achieved, as indicated by the approximate equalization of the total energy flux across the layer (with $^{+4}_{-14}$% deviations from the flux applied at the bottom, see Figure 1).

3. Results

[9] Aside from the latitudinal structure of the wind bands, the turbulent flow fields show substantial temporal variations (see section 4.3). Thus, we express the results in terms of mean quantities represented by $\overline{q}$, where q is a physical variable. The term "mean" stands for averaging longitudinally over a latitude circle and temporally over a period of

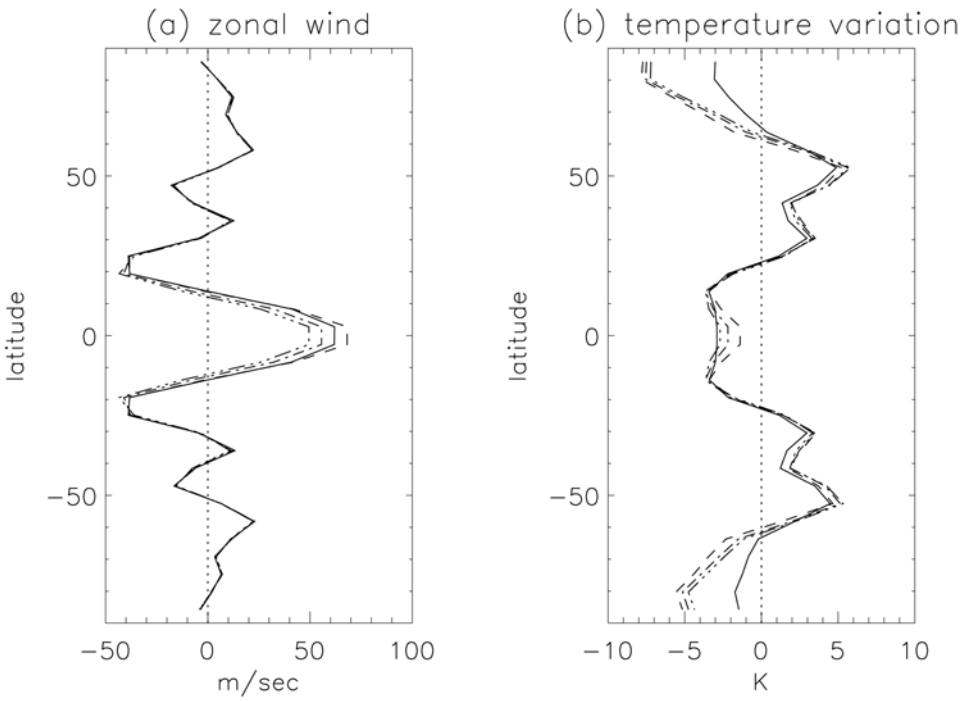

Figure 2. (a) Latitudinal distributions of the mean zonal velocity at four different depths: (1) near the top of the domain (solid curve), (2) near the stable/unstable boundary (dashed curve), (3) near the middle of the unstable layer (dashed-dotted curve), and (4) near the bottom of the domain (dashed-tripple-dotted curve). (b) Latitudinal variations of the mean temperature at the same four depths represented by the same styles of curves.

about 50 Earth years. Thus, q can be written as $q = \overline{q} + q'$ where $\overline{q}$ depends only on latitude and radius. The long-averaging period is needed for statistical convergence, especially for the Reynolds stress [see *Chan*, 2001].

3.1. Energy Fluxes

[10] Figure 1 shows the latitudinally averaged mean energy fluxes (normalized by the input flux, presented by the dotted line for comparison) plotted versus fractional radius. The solid curve shows the total flux, which is composed of several parts: (1) enthalpy flux (dashed curve), (2) radiative/diffusive flux (dashed-dotted curve), (3) flux of kinetic energy (dashed-tripple-dotted curve), and (4) viscous flux. The readers are referred to *Chan and Sofia* [1989] for a detailed discussion of these fluxes. Since the applied kinematic viscosity is very small, the viscous flux is negligible. The enthalpy flux describes the thermal energy carried by convection. It is the dominant form of energy transport in the convection zone, and it turns negative in the stable layer because of overshooting. On the other hand, radiation is the primary form of energy transport in the stable layer. In the region just above the convection zone, in order to counterbalance the negative convective flux, the radiative energy flux has to turn greater than the mean total flux. Inside the convection zone, the diffusive flux is due to the entropy diffusion associated with a very small negative radial gradient of potential temperature.

[11] An interesting result shown in Figure 1 is the substantial magnitude of the kinetic energy flux. This is related to the up-down asymmetry of the stratified compressible gas. Kinetic energy production by buoyancy maximizes near the top of the convection zone [*Chan and Sofia*, 1989]. Before dissipation, it is transported to the lower region. For nonrotating compressible convection, the significance of this flux has been known for a long time [e.g., *Hurlburt et al.*, 1994]. But it is surprising that the maximum of this flux still reaches 44% of the total flux in the present fast rotating case.

[12] Inside the convection zone, the mean temperature structure is very close to adiabatic. The gradient of the mean potential temperature shows some fluctuations, but they are within ±0.15 K/km. This almost adiabatic region extends beyond the convection zone to the height of 1.5 bar. The total variation of potential temperature within this region is less than 1.1 K.

3.2. Zonal Wind and Temperature Bands

[13] Figure 2a shows the latitudinal profiles of the mean zonal wind, $\overline{u}$, at four levels: (1) at the layer near the top of the computed domain at 1.2 bar (solid curve), (2) at the top of the convection zone (dashed curve), (3) in the middle of the convection zone (dashed-dotted curve), and (4) near the bottom of the computed domain (336 bar; dashed-tripple-dotted curve). The latitudinal profiles are close to each other and show an alternating zonal wind pattern with a prominent prograde jet at the equator. The equatorial jet speed is largest at the top of the convection zone (the stable/unstable interface), and it slightly decreases toward the interior (as well as outward). The width of this jet (defined by the zero velocity latitudes), about 27°, is comparable to the observed value on Jupiter. The jet speed, around 70 m/s, is about a factor of 2 lower than the observed values [*Porco et al.*,

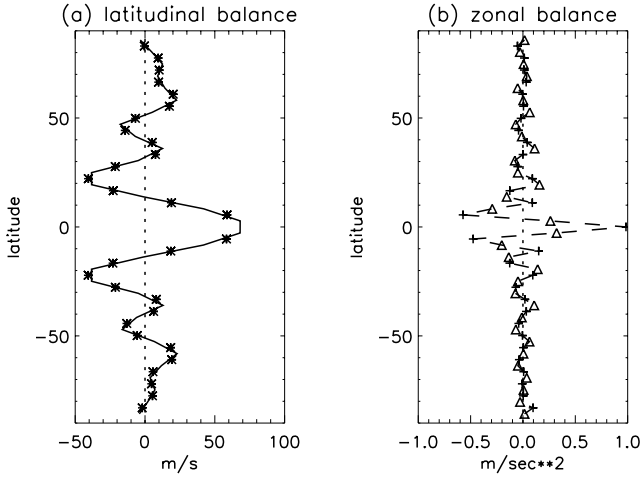

Figure 3. (a) Latitudinal momentum balance satisfies the geostrophic relation. The solid curve shows the mean zonal wind at a layer near the stable/unstable boundary. The asterisks show the pressure gradient term as discussed in the main text with equation (1). (b) Radially integrated zonal momentum balance is mainly between the convergence of the zonal latitudinal Reynolds stress and the Coriolis force associated with the mean vertical velocity. The left and right sides of equation (2), both multiplied by the factor $10^7/\int\overline{\rho}r^2dr$, are shown with pluses and triangles, respectively.

2003]. At other latitudes, the mean zonal winds essentially do not change with depth. The wind pattern is further characterized by the presence of two strong retrograde jets adjacent to the equatorial jet, which is in qualitative agreement with observations. Their velocities reach about −40 m/s. Compared to the observations, the alternating jets at the higher latitudes are too wide in width and too few in number. This may be due to the low number of Gaussian points (order of spherical harmonics) in the numerical spectral model.

[14] The latitudinal profiles of the temperature fluctuations, $\overline{T_1}$, at the same four levels are shown in Figure 2b with the same line styles. Again, the profiles are close to each other; the temperature fluctuations are almost the same at different depths. Some smoothing shows up only at the 1.2 bar level (solid line). Even though there is some similarity in the patterns, in particular the equatorial valley, the amplitudes of the latitudinal variations (∼±5 K) are considerably larger than those observed in Jupiter's troposphere at about 250 mbar [*Simmon-Miller et al.*, 2006]. However, the difference in pressure levels makes the comparison uncertain.

3.3. Momentum Balance

[15] At almost all latitudes (except the equator), the latitudinal momentum balance closely follows the geostrophic relation

$$\overline{u} = \frac{1}{2\Omega\cos(\theta)\overline{\rho}r}\frac{\partial\overline{p}}{\partial\theta}, \qquad (1)$$

where θ is the colatitude. Figure 3a shows a comparison of the left side (solid line) and right side (asterisks) of this equation at the top level of the convection zone. The agreement is very good.

[16] In the zonal momentum balance, discussed with Figure 3b, the terms are small and the fluctuations are large; the balance is more subtle. Since the mean zonal wind and temperature fluctuations are almost independent of depth, one can focus on the horizontal transports. After taking the radial integral of the momentum equation, we find that the balance is primarily between the latitudinal convergence of the zonal latitudinal Reynolds stress and the Coriolis force associated with the vertical (radial) velocity,

$$-\frac{1}{r\sin\theta}\frac{\partial}{\partial\theta}\left[\sin(\theta)\int\overline{\rho uv}\,r^2dr\right] \approx 2\Omega\sin(\theta)\int\overline{\rho w}\,r^2dr. \qquad (2)$$

Here u, v, and w are the zonal, latitudinal, and vertical velocities, respectively. (Note that in this paper the term 'Reynolds stress' is used in a generalized sense, it includes contributions from both the mean velocities and the velocity fluctuations. Generally the later dominates.) The mean vertical velocity is very small (the maximum has a value about 0.001 m/s), but the Coriolis force it generates is the only significant term to balance the convergence of the Reynolds stress. The Coriolis term $2\Omega\cos(\theta)\int\overline{\rho v}r^2dr$ is close to zero (as it should be because of mass conservation). Since ν is small, the viscous stress due to latitudinal shearing of the zonal velocity is negligible. Figure 3b compares the left side (pluses) and the right side (triangles; negative of the Coriolis force) of the equation above. All the numbers have been multiplied by the factor $10^7/\int\overline{\rho}r^2dr$ so that the results are in m/s^2. The dashed curve connects adjacent points to guide the eyes. Approximate balance is illustrated.

4. Discussion

[17] Compared with the earlier models of *Christensen* [2001], *Aurnou and Olson* [2001], and *Heimpel and Aurnou* [2007], referred to as CAOH later, our model is not as deep, and it does not have the high horizontal resolution to simulate the circulation in detail. Our model however implements a realistic physical configuration. It is useful to put it in proper perspective.

4.1. Resolution

[18] The current model is not a direct numerical simulation (DNS) such as those computed by CAOH. Since the rotation is fast, a T20 truncation in the spherical harmonics can barely resolve the very large scales of motions. Figure 4 provides an illustration of the horizontal flow field at the top of the convection at one instance. One may only consider the present model as a large eddy simulation (LES) with the lowest possible resolution. This is a price paid for pursuing the implementation of realistic energy flux and stratification (section 2).

[19] To obtain some idea about the behavior of the model under a change of resolution, we have computed a higher-resolution model (T84, same vertical levels) for a short period of time. Continuing from the low-resolution run, both the higher- and low-resolution models ran for an additional 32 Earth days. Figure 5 shows a comparison of the resultant mean zonal wind profiles at three different

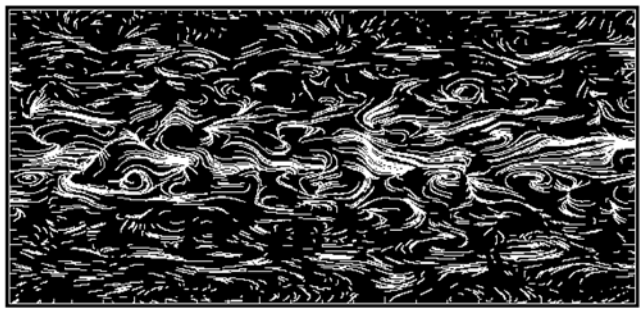

Figure 4. An example of pseudostreamlines illustrating the horizontal flow field at the top of the convection zone. The y axis is $-90°$ to $90°$ latitude, and the x axis is $-180°$ to $180°$ longitude. The low resolution limits the motions to large scales. As a consequence, the significance of the large-scale eddies is overrepresented. The eddy kinetic energy is about 1.4 times that of the mean zonal wind. The factor is larger than estimates on the basis of observation of Jovian clouds.

depths. The temporal average is over the last 10 days of the integration period. The higher- and low-resolution cases are separately represented by the curves and the discrete symbols. These short runs cannot be used to test the convergence of resolution. They only show that the motions in smaller scales do not disrupt the jets in a dynamical time scale, $L/V \sim 10$ Earth days (if the characteristic length, L, and velocity, V, are taken to be the planetary radius and maximum wind speed at the equator, respectively). At the top layer, the equatorial jet of the higher-resolution case develops a dip at the center. Similar behavior has also been found in some instances of a finite difference regional LES experiment [*Chan*, 2006].

4.2. Viscosity

[20] The viscosity used in the current model is higher than the value for the real gas, but it is still sufficiently small to produce a large Taylor number, 2.7×10^{13}, and a large Reynolds number, $LV/\nu \sim 10^9$ (with L and V defined in section 4.1). However, these values do not carry the same numerical meanings as those of previous models. Generally, viscosity is enhanced to provide numerical stability. The stability problem is usually caused by the particular treatment or implementation of advection in physical space, and the stability criterion is that the grid Reynolds number $VL/(N\nu)$ should be $\leq$O(1) (N is a representative number of grids in a single dimension). Therefore, viscosity can only be decreased by increasing N (higher resolution), and high values of Reynolds, Taylor, and Rayleigh numbers (all having viscosity in the denominator) can only be achieved by high-resolution calculations. In the present model the resolution is low, but the numerical method allows for a small viscosity without invoking a hyperviscosity. Because of the nonaliasing transforms that make equivalent the computations of quadratic advection terms in spectral and physical spaces, the transformed spectral model behaves like a truncated spectral model (a set of coupled ordinary differential equations for a finite number of spectral coefficients). For the barotropic case, the conservation of total energy and total enstrophy constrain the spectral coefficients of a truncated spectral model [*Machenhauer*, 1979]. Stable computations can be made without viscosity. A test of this property for the code has been discussed by *Chan et al.* [1994, section 4a]. In the current application, the situation is baroclinic. The stability of the present model was verified empirically.

[21] In the present model, the high values of Taylor, Reynolds, and Rayleigh numbers are due to the presence of a low viscosity that works numerically. The Rossby number Ro (= $V/\Omega L$), on the other hand, does not depend on the viscosity and is a more meaningful parameter that describes the intrinsic properties of the flows. Using the computed equatorial jet speed for V and the planetary radius for L, Ro is on the order of 0.01.

4.3. Domain Depth

[22] Even though the setting of the present model is convective, its thickness differs from those of the earlier convective models in a significant manner. A consequence is that the horizontal components of velocity are much larger than the vertical one. In the current model the root-mean-square vertical velocity is about 300 times smaller than those of the horizontal velocities (same order of magnitude as the domain aspect ratio, width/depth). The mean vertical velocity is another 3 orders of magnitude smaller. The mean zonal wind and the mean latitudinal temperature variations are almost independent of depth. In this sense, the model is almost two-dimensional.

[23] In the earlier deep convection models, the tangent cylinders to the inner boundaries play an important role in determining the width of the equatorial jet (as the approximate location of maximum retrograde zonal wind). In the

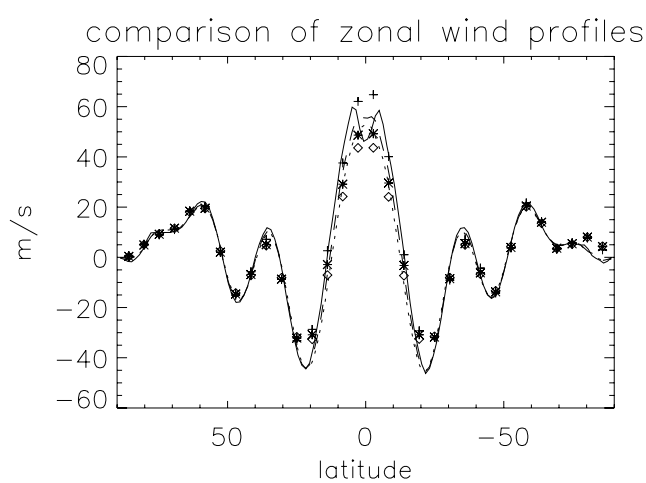

Figure 5. Comparison of latitudinal distributions of the mean zonal velocity between the higher-resolution (curves) and low-resolution cases (discrete symbols). The distributions are plotted for three different depths: (1) at the top of the convection zone (solid curve and pluses), (2) in the middle of the convection zone (dashed curve and asterisks), and (3) near the bottom of the convection zone (dotted curve and diamonds). Starting from the same initial model, the two cases ran separately for a period of 32 Earth days. An average over the last 10 model days is used to obtain the mean velocities.

Table 1. Computed Cases

Case	Depth (km)	p_{bottom} (bar)	ν (m^2/s)	Levels	Mean u_{eq}[a](m/s)	Standard Deviation u_{eq}[a](m/s)
A	(1/3) × 430	25	5.6	23	44	9.4
B	(2/3) × 430	119	2 × 5.6	44	50	7.4
C	(2/3) × 430	119	5.6	44	51	7.3
D	430	340	5.6	68	69	7.0

[a]Averaged over a period of 2500 Earth days only.

present model, the width of the equatorial jet is much larger than the angular span between the intersections of the tangent cylinder with the outer sphere. The tangent cylinder does not dictate the width of the equatorial jet. Rather, the widths of the jets are compatible with the Rhines scaling, as what happens in two-dimensional turbulence models. The shallowness of the current model have made it qualitatively different from the deep convection models. The change in regime may be understood by considering a Rossby number Ro' that uses the depth of the domain as length scale. In order to set up Taylor column rolls outside the tangent cylinder, Ro' should also be much less than 1. In the current model, Ro' is about 1. Within the region outside the tangent cylinder, the Coriolis force is not strong enough to dominate over the inertial force.

[24] Even though the current model is thin, the finite thickness and convection still makes it much different from conventional two-dimensional models. Recent simulations of compressible convection in boxes with tilted rotation vectors [*Chan*, 2001; *Käpylä et al.*, 2004] have shown that for small Rossby numbers ($Ro < 1$) there is a convergence of radially and longitudinally integrated Reynolds stress (zonal latitudinal component) toward the equator. This can drive an overall superrotation at the equator. The balance of the radially integrated mean zonal momentum is made possible by the presence of Coriolis force associated with the vertical velocity (section 3.3).

[25] Before the current model was computed, several shallower models had been explored. The specifications of the models are given in Table 1. Only the domain depth, viscosity, and number of vertical levels vary. All other parameters are the same. The current model is listed as case D. Column 3 shows the pressure at the bottom of the domain. Its magnitude grows much faster than the domain depth; so does internal energy. The required time for thermal relaxation (discussed in section 2) grows accordingly.

[26] All the models show superrotating equatorial jets and alternating winds. The temporally and longitudinally averaged means and standard deviations (sd) of the equatorial zonal wind at the top of the convection zone, over a period of 2500 Earth days, are also listed in the table. The jet strength increases and its variability decreases as the domain depth increases (see Figure 6). In this paper, we have chosen the deepest case, D, to discuss in detail. Comparing cases B and C shows that the change in viscosity did not produce significant differences.

5. Summary

[27] With realistic values of some key physical parameters applied to a thin shell of convecting gas, stratified and compressible, this model produces the following features: (1) alternating wind bands, (2) dominant positive equatorial jet, (3) two strong negative jets adjacent to the equatorial jet, (4) small latitudinal temperature variations, and (5) geostrophic balance. (6) The balance of the vertically integrated zonal momentum is primarily between the latitudinal convergence of the zonal latitudinal component of Reynolds stress and the Coriolis force associated with vertical motions. The first five are similar to the results obtained earlier through the study of incompressible convection. The compressibility and stratification in the present model do not seem to introduce significant effects. On the other hand, the shallowness of the current model makes it different from the earlier convective models. The small domain depth prevents the formation of Taylor column cells outside the tangent cylinder. The equatorial acceleration in the model occurs through the convergence of the stress component $\overline{\rho uv}$. It is counteracted by the Coriolis force associated with the mean vertical velocity. It would be valuable to investigate how the transition may occur from the shallow to the deep behavior. But that will require deeper models and much more computer time. It is beyond the scope of the present paper.

[28] The comparison of our results with observations shows only qualitative agreement. The equatorial jet is still too weak, and the alternating jets are too few in number. The latitudinal temperature variation seems a little high, but there are no direct observations to compare with. Considering the simplifications introduced (e.g., ignoring solar heating and chemical processes), and the low resolution required to make the computation feasible, the order of magnitude agreements are still encouraging. The improvement of spatial resolution, increase of model depth, and inclusion of solar heating are areas that need to be attended to in the future.

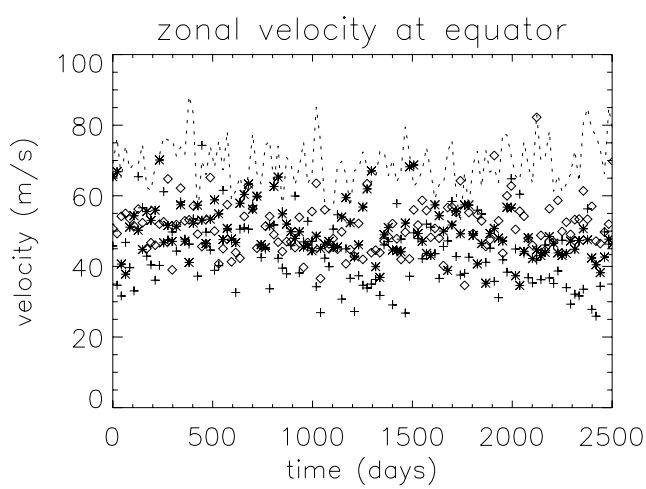

Figure 6. Temporal variations of the equatorial jet speed (zonal wind averaged over the equator) at the top of the convection zone. The pluses, asterisks, diamonds, and the dotted curve show the results for cases A, B, C, and D, respectively. The variations exhibit the existence of some long time scales.

[29] **Acknowledgments.** K.L.C. thanks the Hong Kong Research Grants Council for support. The manuscript has been much improved by the reviewers' insightful comments.

References

Aurnou, J. M., and P. I. Olson (2001), Strong zonal winds from thermal convection in a rotating spherical shell, *Geophys. Res. Lett.*, *28*, 2557–2559.

Busse, F. H. (1976), Simple model of convection in Jovian atmosphere, *Icarus*, *29*, 255–260.

Chan, K. L. (2001), Rotating convection in f-planes: Mean flow and Reynolds stress, *Astrophys. J.*, *548*, 1102–1117.

Chan, K. L. (2006), A finite-difference convective model for Jupiter's equatorial jet, in *Convection in Astrophysics: Proceedings of the 239th Symposium of the International Astronomical Union*, edited by F. Kupka et al., pp. 230–232, Cambridge Univ. Press, New York.

Chan, K. L., and S. Sofia (1986), Turbulent compressible convection in a deep atmosphere: III. Tests on the validity and limitation of the numerical approach, *Astrophys. J.*, *307*, 222–241.

Chan, K. L., and S. Sofia (1989), Turbulent compressible convection in a deep atmosphere: IV. Results of three-dimensional computations, *Astrophys. J.*, *336*, 1022–1040.

Chan, K. L., H. G. Mayr, J. G. Mengel, and I. Harris (1994), A "stratified" spectral model for stable and convective atmospheres, *J. Comput. Phys.*, *113*(2), 165–176.

Cho, J. Y. K., and L. M. Polvani (1996), The morphogenesis of bands and zonal winds in the atmospheres on the giant outer planets, *Science*, *273*, 335–337.

Christensen, U. R. (2001), Zonal flow driven by deep convection in the major planets, *Geophys. Res. Lett.*, *28*, 2553–2556.

Galperin, B., H. Nakano, T. P. Huang, and S. Sukoriansky (2004), The ubiquitous zonal jets in the atmospheres of giant planets and Earth's oceans, *Geophys. Res. Lett.*, *31*, L13303, doi:10.1029/2004GL019691.

Heimpel, M., and J. Aurnou (2007), Turbulent convection in a rapidly rotating spherical shell: A model for equatorial and high latitude jets on Jupiter and Saturn, *Icarus*, *187*, 540–557.

Hurlburt, N. E., J. Toomre, J. M. Massaguer, and J.-P. Zahn (1994), Penetration below a convective zone, *Astrophys. J.*, *421*, 245–260.

Ingersoll, A. P., and D. Pollard (1982), Motion in the interiors and atmospheres of Jupiter and Saturn: Scale analysis, anelastic equations, barotropic stability criterion, *Icarus*, *52*, 62–80.

Ingersoll, A. P., P. J. Girasch, D. Banfield, A. R. Vasavada, and the Galileo Imaging Team (2000), Moist convection as an energy source for the large-scale motions in Jupiter's atmosphere, *Nature*, *403*, 630–632.

Käpylä, P. J., M. J. Korpi, and I. Tuominen (2004), Local models of stellar convection: Reynolds stresses and turbulent heat transport, *Astron. Astrophys.*, *422*, 793–816.

Machenhauer, B. (1979), The spectral method, in *Numerical Methods Used in Atmospheric Models*, *GARP Publ. Ser.*, vol. 17, pp. 121–275, Global Atmos. Res. Programme, World Meteorol. Organ., Geneva.

Marcus, P. S., T. Kundu, and C. Lee (2000), Vortex dynamics and zonal flows, *Phys. Plasmas*, *7*, 1630–1640.

Mayr, H. G., I. Harris, and K. L. Chan (1984), Differential rotation in a solar-driven quasi-axisymmetric circulation, *Earth Moon Planets*, *30*(3), 245–274.

Porco, C. C., et al. (2003), Cassini imaging of Jupiter's atmosphere, satellites, and rings, *Science*, *299*, 1541–1547.

Rhines, P. B. (1975), Waves and turbulence on a beta-plane, *J. Fluid Mech.*, *69*, 417–443.

Showman, A. P., P. J. Gierasch, and Y. Lian (2006), Deep zonal winds can results from shallow driving in a giant-planet atmosphere, *Icarus*, *182*, 513–526.

Simmon-Miller, A. A., B. J. Conrath, P. J. Gierasch, G. Orton, R. K. Achterberg, F. M. Flasar, and B. Fisher (2006), Jupiter' atmospheric temperatures: From Voyager IRIS to Cassini CIRS, *Icarus*, *180*, 98–112.

Sun, Z. P., G. Schubert, and G. A. Glatzmaier (1993), Banded surface flow maintained by convection in a model of the rapidly rotating giant planets, *Science*, *260*, 661–664.

Williams, G. (1978), Planetary circulations: 1. Barotropic representation of Jovian and terrestrial turbulence, *J. Atmos. Sci.*, *35*, 1399–1426.

Yano, J. I., O. Talagrand, and P. Drossart (2003), Outer planets: Origins of atmospheric zonal winds, *Nature*, *421*, 36.

Zhang, K., and G. Schubert (2000), Teleconvection: Romotely driven thermal convection in rotating stratified spherical layers, *Science*, *290*, 1944–1947.

K. L. Chan, Department of Mathematics, Hong Kong University of Science and Technology, Clear Water Bay, Hong Kong, China. (maklchan@ust.hk)

H. G. Mayr, NASA Goddard Space Flight Center, Code 910.4, Greenbelt, MD 20771, USA.